npj | quantum information

Article

Published in partnership with The University of New South Wales

https://doi.org/10.1038/s41534-024-00910-0

Qubit teleportation between a memory-compatible photonic time-bin qubit and a solid-state quantum network node

Mariagrazia Iuliano[1,4], Marie-Christine Slater[1,4], Arian J. Stolk[1], Matthew J. Weaver[1], Tanmoy Chakraborty[1], Elsie Loukiantchenko[1], Gustavo C. do Amaral[1], Nir Alfasi[1], Mariya O. Sholkina[1], Wolfgang Tittel[2,3] & Ronald Hanson[1] ✉

We report on a quantum interface linking a diamond NV center quantum network node and 795nm photonic time-bin qubits compatible with Thulium and Rubidium quantum memories. The interface makes use of two-stage low-noise quantum frequency conversion and waveform shaping to match temporal and spectral photon profiles. Two-photon quantum interference shows high indistinguishability between converted 795nm photons and the native NV center photons. We use the interface to demonstrate quantum teleportation including real-time feedforward from an unbiased set of 795nm photonic qubit input states to the NV center spin qubit, achieving a teleportation fidelity well above the classical bound. This proof-of-concept experiment shows the feasibility of interconnecting different quantum network hardware.

The future quantum internet will leverage the principles of quantum mechanics for ultra-secure communication, enhanced sensing, and distributed quantum computing[1,2]. Progress in the past decade has led to pioneering experiments on different components of such a network[3–7]. For instance, entanglement generation between separated quantum memory systems based on atomic ensembles has recently been reported[8,9] and the first multi-node network of rudimentary quantum processors has been realized inside the lab[10,11]. As different hardware platforms may be optimized for different network tasks, realizing interfaces that enable quantum information transfer between heterogeneous devices is a key challenge.

Here, we report on a proof-of-concept demonstration of a quantum interface between a diamond NV center qubit[12,13] and photonic time-bin qubits at 795nm that are compatible with Thulium-based solid-state memories[14–16] and Rubidium-based atomic gas memories[17–20]. Such an interface conceptually corresponds to future quantum Internet scenarios such as connecting remote qubit processors via a repeater chain[21] or realizing remote state preparation on a quantum computing server from a photonic client[22]. We validate the quantum nature of the interface by performing quantum teleportation[23,24] of 795nm time-bin qubits into the NV center spin qubit with state fidelity beating the classical bound.

A major challenge for linking heterogeneous quantum network hardware is the matching of their corresponding photonic qubits. Many leading hardware platforms for quantum memories and quantum network nodes are based on atom-like systems[25,26]. The properties of the photonic interface of these platforms, such as temporal profile and wavelength of emitted photons, are therefore largely determined by the atomic properties and vary significantly among the different platforms. Our approach to bridging these differences is depicted in the schematic of our interface in Fig. 1.

The interface converts the input 795nm photonic time-bin qubit to match the properties of the NV center photon. In parallel, entanglement is generated between the spin state of the NV center and the temporal mode of a single emitted photon. Then, the converted 795nm photon and the NV photon are interfered on a beam-splitter. Subsequent detection of the photons in different time bins constitutes a Bell state measurement that teleports the original 795nm time-bin qubit state to the NV spin qubit. Real-time feedforward of the Bell-state measurement outcome and application of the corresponding correction gate on the NV spin qubit completes the action of the interface.

For this interface to function with high fidelity, it is crucial that the converted 795nm photons are indistinguishable from the NV center photons. In particular, the 795nm photons need to match the NV photons' 637nm wavelength, polarization and exponential temporal profile set by NV's 12 ns optical lifetime. In this proof-of-concept work, we create photonic time-bin qubits at 795nm from weak coherent states by using an intensity modulator and a phase modulator. We calibrate the intensity modulator to mimic the NV photon's temporal profile within a 30ns time window. The photonic states obtained through this method are compatible

[1]QuTech & Kavli Institute of Nanoscience Delft, Delft University of Technology, Delft, The Netherlands. [2]Department of Applied Physics, University of Geneva, Geneva, Switzerland. [3]Constructor University Bremen GmbH, Bremen, Germany. [4]These authors contributed equally: Mariagrazia Iuliano, Marie-Christine Slater. ✉e-mail: r.hanson@tudelft.nl

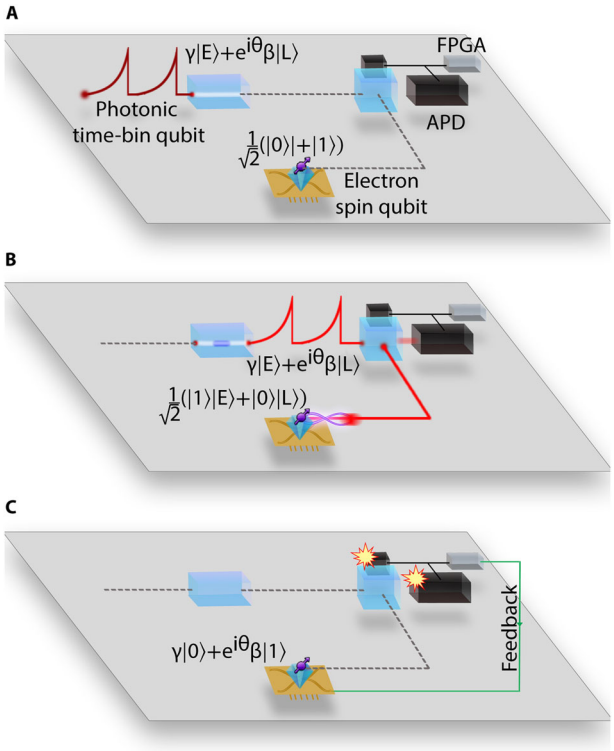

Fig. 1 | Overview of the quantum interface between 795nm photonic time-bin qubits and an NV center processing node. The interface consists of a low-noise two-step frequency conversion module including a frequency stabilization module, an interference station containing a balanced beam splitter with output ports connected to avalanche photodiodes (APDs), and an FPGA for real-time feedback. The interface can be visualized in three steps: **A** a 795nm time-bin qubit with a temporal shape matching the spontaneous emission profile of the NV center is sent to the input of the interface. The NV spin qubit is prepared in a balanced superposition state. **B** The 795 nm photonic qubit is converted to 637 nm (details on the conversion setup are in Fig. 2), while the NV center generates a 637 nm photonic time-bin qubit entangled with the spin qubit. The generation of the 795 nm photonic qubit is timed to ensure maximum overlap at the beam splitter with the NV center photonic qubit. **C** Upon detecting one photon in each time bin, feedback of the correct phase flip to the NV spin qubit of the NV completes the state teleportation. For the experiments reported in this paper, we employed the NV qubit setup, called "Alice,', described in Refs. 10,11, that includes a micro-controller unit (MCU) and a fast waveform generator (AWG). Dashed gray lines represent the optical path.

with the storage and retrieval from Thulium-doped solid-state quantum memories[16,27] as well as Rubidium-gas-based quantum memories[28,29]. These platforms are capable of multiplexing by storage and retrieval of multiple photonic modes in different degrees of freedom[26,30], and therefore have attracted interest for quantum repeater applications[31].

To achieve wavelength indistinguishability, we employ a low-noise two-stage quantum frequency conversion process[32], depicted in Fig. 2A. In the first step, the 795nm shaped weak-coherent state is overlapped with a 1064nm pump laser and coupled into a temperature-stabilized periodically-poled Lithium Niobate (ppLN) waveguide crystal, generating 455nm light via a sum-frequency conversion process with conversion efficiency of 32% (Fig. 2B), measured free-space to free-space between the output of the input fiber and before the coupling into the output fiber. Subsequently, the 455nm light is down-converted to 637nm using a 1596nm pump laser, with conversion efficiency of 22%. At the output of each ppLN crystal we include dichroic mirrors and filters to remove residual unconverted light and pump light. The overall process efficiency including in- and outcoupling from fibers and filtering is 3%, which is sufficient for the current proof-of-concept but should be further improved in future designs. Importantly, having both pump lasers red-detuned from the signal photons results in a negligible amount of added noise in the conversion stages, obtaining a signal-to-noise ratio≥1250, when only the conversion setup is considered. To ensure that the converted light precisely matches the NV photon frequency, despite unavoidable component drifts, the frequency of converted 795nm light is locked to the NV excitation laser light. To this end, an identical two-stage conversion setup is employed with 1 mW at the input derived from the same 795nm source (Fig. 2A). Details on the frequency locking procedure and the employed electronics are discussed in the Supplementary Information. The resulting spread of the beat signal is 75 kHz, pushing the corresponding contribution to teleportation infidelity well below 1% (see below).

Results

Two-photon quantum interference between converted 795nm photons and NV center photons

To investigate the degree of indistinguishability of the NV photons and the converted 795nm photons, we perform a two-photon quantum interference (TPQI) experiment, also known as Hong-Ou-Mandel interference. Perfectly indistinguishable photons interfering on a balanced beam-splitter show bosonic coalescence leading to zero probability of detecting photons in both output ports of the beam-splitter[33]. In such an experiment, on one side we employ the NV center in its negatively charged state NV^-. The ground state of NV^- is a spin-1 system whose spin sublevels are split by the zero-field splitting and the applied magnetic field of 25.3 mT[12]. We employ the m_S= 0 (-1) spin state as the $|0\rangle$ ($|1\rangle$) qubit state. The NV optical transitions are spin-dependent, allowing for spin-selective optical excitation and photon emission. In the current work, we use the cycling transition $|0\rangle \rightarrow |g\rangle$, where $|g\rangle$ represent the $|E_x\rangle$ excited state. In the TPQI experiment, the NV center can be modeled as a single-photon source parametrized by the probability of a photon detection per optical excitation p_{NV} (counts per shot).

On the other side, the 795nm photonic states constitute a multi-photon source, featuring Poissonian photon statistics. Up to the second order, the emission probability can be approximated through the mean-photon number $|\alpha|^2$ as $|\alpha|^2 + 1/2|\alpha|^4$ [34]. The consequences of having two photonic sources with different statistics are discussed in detail in the SI.

In Fig. 3A, the experimental sequence for the TPQI experiment is depicted. In the first step, a Charge-Resonance (CR) check is performed[35], which ensures that the NV center is in the correct charge state (namely, NV^-) and the lasers are on resonance with the relevant NV transitions. When the CR check threshold is satisfied, the actual TPQI experiment is triggered. Two trains of 10 optical π-pulses each, which we define as 10 different bins, are sent to the NV, which leads to 20 possible emission windows (10 per train). Each train is preceded by an optical spin-reset pulse that prepares the NV in the $|0\rangle$ state. In parallel, two trains of 10 decay-shaped pulses each are sent from the 795nm laser. The mean-photon number can be manipuleted via a variable optical attenuator (VOA). As illustrated in Fig. 3A, the first train of pulses constitutes the indistinguishable sequence, with the two photonic states overlapping in time on the beam splitter. The second train is the distinguishable sequence: each 795nm photonic state is delayed by 50ns with respect to the corresponding NV photon, rendering the photons fully distinguishable. The sequence of two trains is repeated 100 times before returning to the CR check. The next CR check validates both the previous TPQI sequence and, in case the threshold is satisfied, directly triggers the next sequence. In case the validation round of CR check fails, the experiment iteration is discarded in the analysis, while the CR check is repeated until success to trigger the next experiment iteration. The emitted photons from both sides impinge on a 50:50 in-fiber beam splitter, whose output ports are connected to two single-photon detectors. A timetagger registers the detection times of the photons in the two output ports, enabling the reconstruction of the histograms in Fig. 3B. Each bin of the histogram counts the number of coincident clicks in the two beam splitter output arms for the respective bin differences.

From the histograms in Fig. 3B we extract the visibility $V=1-\frac{p_{ind}}{p_{dist}}$, where p_{ind} (p_{dist}) is the probability of a coincidence detection if the photons are indistinguishable (distinguishable) in the 0-bin difference. Taking into account that the photonic states follow different statistics and introducing

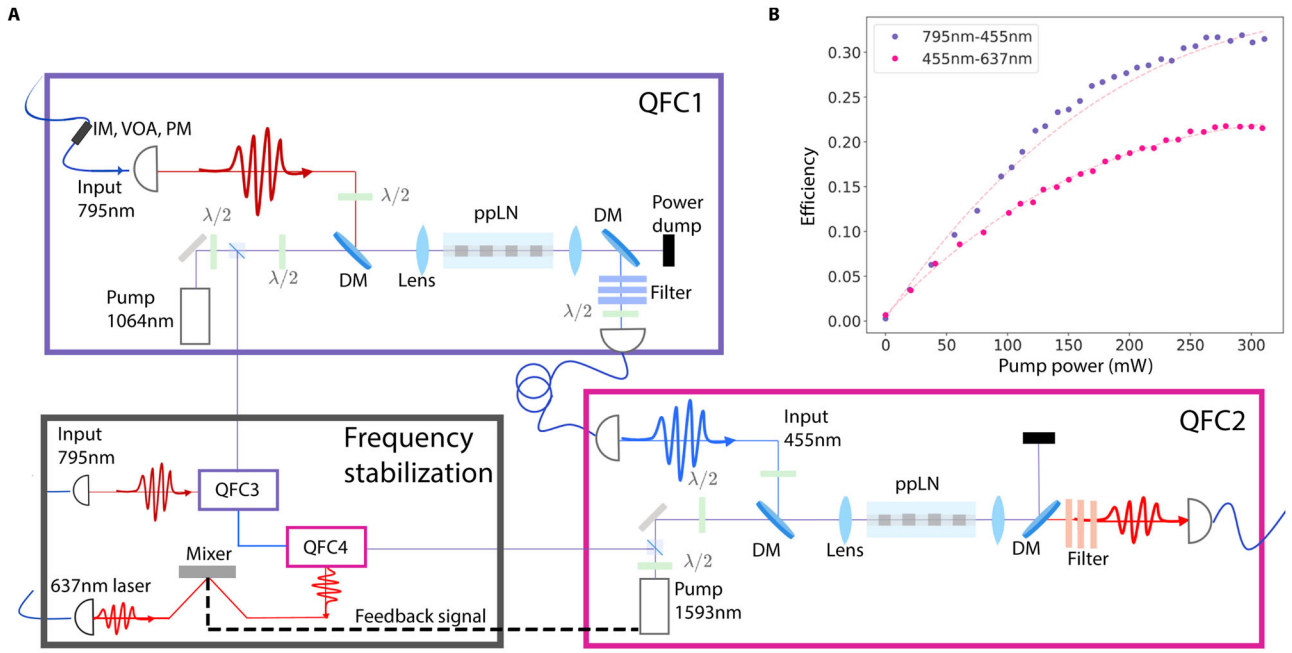

Fig. 2 | Quantum frequency conversion setup. A Overview of the frequency conversion setup. To generate converted weak-coherent states at 637nm, the input light at 795nm undergoes two-step frequency conversion (QFC1 and QFC2), after passing through an intensity modulator (IM) to obtain the typical decay time-shape of the NV spontaneous emission, a variable optical attenuator (VOA) to manipulate the mean photon number, and a phase modulator (PM) for imprinting a phase on the time-bin qubits (only for quantum teleportation experiments). At the output of each conversion step, a dichroic mirror (DM) and a set of filters suppress residual unconverted light and pump light. A copy of the two-step frequency conversion setup (QFC3 and QFC4) is used for frequency stabilization. A higher power tap-off from the 795nm laser is converted and the resulting 637nm light is mixed with the light coming from the excitation laser of the NV. An error signal is computed and fed back to the frequency modulator of the 1593nm pump laser to match the converted light to the excitation wavelength of the NV. **B** Measured efficiency for each step of the conversion while sweeping the power of the corresponding pump laser. The dashed lines represent the respective fit of the data points to a saturation curve, to extrapolate the optimal pump power, that in both cases is 310 mW. The relative error on each data point is 1%.

the indistinguishability η, the visibility can be expressed as

$$V = \frac{\eta x}{\frac{1}{2}g^{(2)}(0) + \frac{1}{2}x^2 + x + \frac{2p_{noise}(1+x)}{p_{NV}} + \frac{2p_{noise}^2}{p_{NV}^2}} \quad (1)$$

(see SI for the derivation), where x is the ratio $|\alpha|^2/p_{NV}$ and p_{noise} is the probability of a background (noise) click per 30ns window in one detector.

By performing the TPQI experiment and extracting the visibility for 6 different values of x, we can reconstruct the visibility function as shown in Fig. 3C. We also plot the expected visibility function, using the independently measured values for the NV $g^{(2)}$ of 0.011 ± 0.004 and p_{NV} of (5.76 ± 0.20)e^{-4}, for several values of η. The value of p_{noise} is discussed in the SI. We observe that the data follows the model closely over the full range. From a fit to the data we obtain the indistinguishability η=(0.895 ± 0.019), showing that we have matched all the relevant degrees of freedom of the two photonic states to a high level. The limited indistinguishability can be due to a residual mismatch between the temporal profile of the NV photons and the 795nm photons, as well as an imperfect coherence of the NV photons, that from previous NV-NV TPQI experiments showed limited indistinguishability of 0.9[10].

Qubit teleportation from a 795nm photonic time-bin qubit to the NV center spin qubit

Having established the high indistinguishability of the photonic states involved, we exploit the interface to perform quantum teleportation of 795nm time-bin qubits to the NV electron spin qubit, as illustrated in the diagram in Fig. 4A. Real-time feed-forward is included to complete the teleportation, enabling the correction of phase-flipped outcomes in the Bell-state measurement and delivery of the teleported state "alive".

The 795nm time-bin qubit is constituted by an early and late weak-coherent state separated by 300 ns and generated in the same way as in the TPQI experiment. Additionally, we include a phase modulator (PM) to manipulate the phase difference between the early and late temporal modes. The resulting qubit state is therefore in the general form of $\gamma|E\rangle + e^{i\theta}\beta|L\rangle)$ with $|E\rangle$ ($|L\rangle$) denoting the early (late) time bin. For this experiment, we prepare time-bin qubits in an unbiased set of states (the cardinal states) that we indicate as: $|Z\rangle$, $|-Z\rangle$, $|X\rangle$, $|-X\rangle$, $|Y\rangle$, $|-Y\rangle$, referring to their position on the Bloch sphere.

On the NV's side, the electron spin qubit is optically initialized in $|0\rangle$. A microwave $\pi/2$ rotation along $\hat{x}$ axis of the Bloch sphere brings the qubit into a balanced superposition state. An optical π-pulse excites the NV's population in $|0\rangle$, enabling the spontaneous emission of a photon in the early time bin. Subsequently, the electron spin goes through a microwave π rotation along $\hat{y}$ axis, and another optical π- pulse enables the NV to spontaneously emit the late time-bin photon. The resulting NV-photon entangled state is $1/\sqrt{2}(|1\rangle|E\rangle \pm |0\rangle|L\rangle)$. Throughout the teleportation experiment we keep the ratio $|\alpha|^2/p_{NV}$ constant at 1.20 ± 0.24 by regular recalibration.

The converted 795nm photonic state and the NV photon interfere on the balanced beam splitter, erasing the which-path information. Successful teleportation is heralded by the detection of a photon in each of the two time-bins. We can discriminate between the Bell states $|\Psi^+\rangle$ and $|\Psi^-\rangle$ by the double-click pattern: two clicks on the same detector for $|\Psi^+\rangle$ and two clicks on two different detectors for $|\Psi^-\rangle$. The valid detector clicks are detected by an FPGA in a 50ns window around the corresponding photons' time of arrival. In data analysis, we further shorten the valid teleportation time window to 20ns for an improved signal-to-noise ratio. The teleportation sequence is repeated for a maximum of 50 times before going back to the CR check.

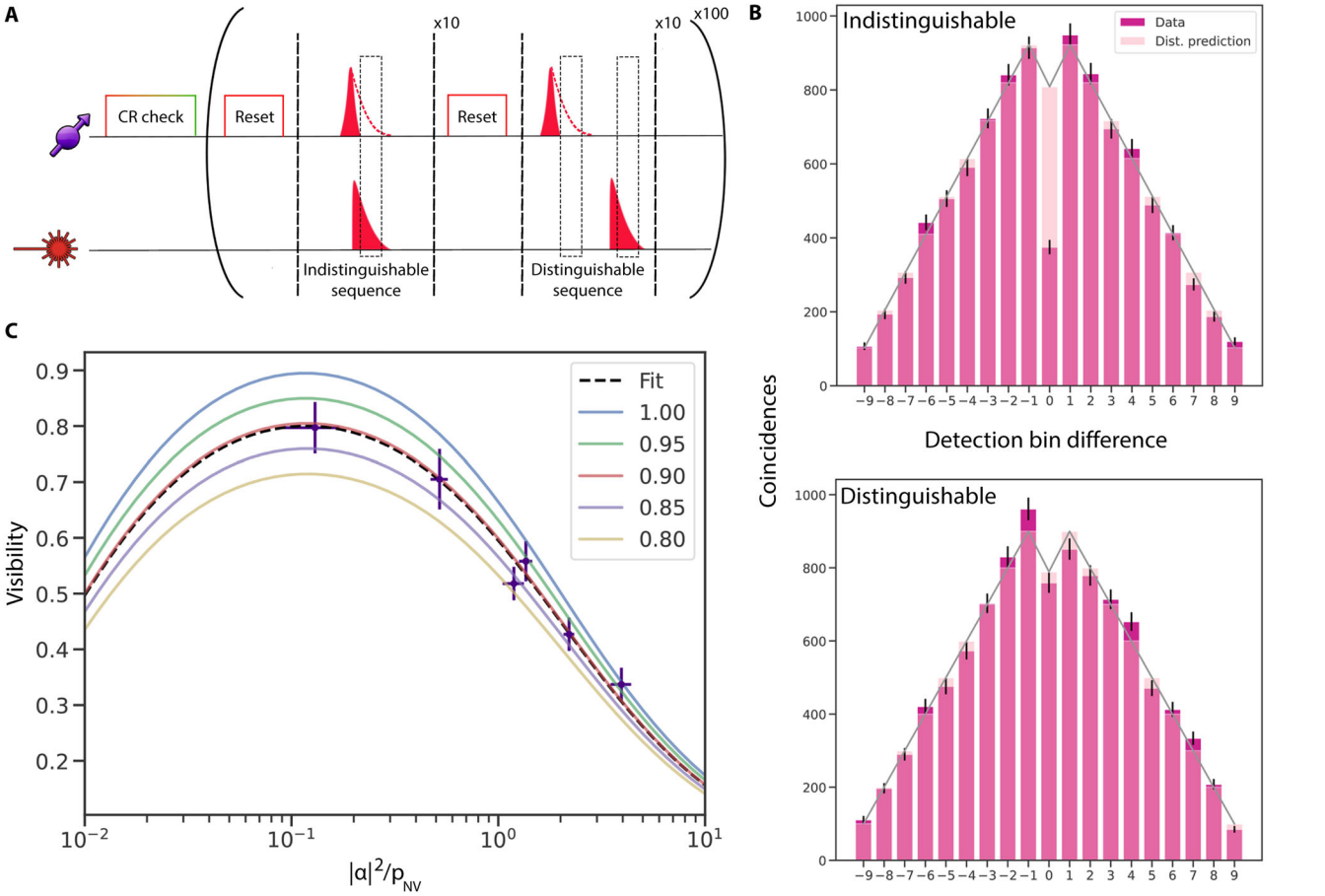

Fig. 3 | Two-photon quantum interference. A Experimental sequence for the two-photon quantum interference experiment. The top line refers to the NV, while the bottom refers to the 795nm weak-coherent state. Dashed lines represent the spontaneous emission of single photons, while filled lines represent coherent light emission. **B** Histograms of the coincident clicks in the two sequences (magenta) for the ratio $x = |\alpha|^2/p_{NV}$ of 1.19 ± 0.14. Each bar of the histograms represents coincident clicks in the two detectors within 30ns windows for all the possible combinations of a given time bin difference. As a reference, we also include, in both histograms, the expected coincidences in the case of perfectly distinguishable photons (in pink). In both diagrams, the gray line connects the expected values of the distinguishable prediction. In the distinguishable case, we consider two pulse windows: one around the NV photons and one around the converted 795nm photonic states. Therefore, the histogram contains the contribution of coincident clicks for three possible cases: coincident clicks in the NV window, in the converted 795nm window and in the combined windows. **C** Extracted visibility for different values of x. The values are fitted according to the visibility model included in the SI. The error bars (1σ) on the horizontal axis are obtained by propagating the errors from directly measuring $|\alpha|^2$ and p_{NV} in the distinguishable sequence and computing the ratio, whereas the vertical error bars are obtained via error propagation on the visibility formula. The dashed line represents the fit result, corresponding to indistinguishability of 0.895 ± 0.019, while the colored lines show our model of the visibility for different values of indistinguishability.

When the FPGA detects a valid click pattern, it sends a two-bit message to the AWG. The AWG jumps out from the teleportation attempt sequence (Fig. 4A) and starts the feedback and tomography sequence for the electron spin state. This sequence is composed of an XY4 dynamical decoupling sequence[36] followed by a basis selection pulse for the tomography. The latter is selected in real-time, taking the detector click pattern into account by applying a phase-flip correction when necessary. Finally, a single-shot readout of the NV spin qubit is performed. Throughout the measurement, a set of automated measurement and calibration routines detect anomalies in the converted frequency and in the reset frequency, declaring those datasets as failed when the required parameters are not met (more details in the SI). In Fig. 4B, the results for the teleportation of the six cardinal states are reported together with the average state fidelity. The average fidelity is obtained as $F_{avg}=1/3\bar{Z}+1/3\bar{X}+1/3\bar{Y}$, where $\bar{Z}$, $\bar{X}$, $\bar{Y}$ represent the average fidelity along the respective axis. The resulting fidelity of (75.5 ± 1.0)%. is well above the classical bound, which is set taking into account the use of a multi-photon source (see SI). Additionally, we also calculate the average fidelity for the equatorial states in the absence of feed-forward. In this case, the fidelity is consistent with a fully mixed state, confirming the critical role of feedback in the teleportation protocol. In the measured fidelities, we also filter based on the CR check's validation.

In Fig. 4C we report the comparison between the measured fidelities and the predicted values of our model as a function of the ratio $|\alpha|^2/p_{NV}$. The model includes the effect from leakage of the intensity modulator, resulting in a preparation error for the Z states of around 4%. In general, the Z states only require classical correlations for the teleportation to work while teleportation of the X, Y states also depends on the phase coherence, leading to sensitivity to different error sources. As the most relevant error sources in our work (double NV excitation, imperfect photon indistinguishability, imperfect preparation of the photonic time-bin qubit's phase and the fact that the photonic qubit is not a true single photon) all affect the phase coherence but not the classical correlations, the Z states maintain much higher fidelity than the X, Y states. More details on the simulated curves and the error sources are included in the SI. The small discrepancy between the X and Y data points and the simulation may be due to errors not captured by the model. On one side, the model does not consider imperfections in the microwave pulses that implement the NV quantum gates, which we estimate to cause an accumulated error below 1.5%. On the time-bin qubit side, our model does not take into account phase errors due to imperfections in the fast phase modulation, which affect the preparation of the X and Y states. Correcting for the input photonic qubit preparation errors for the Z states yields a best estimate for the teleportation fidelity of (78.3 ± 0.9)%.

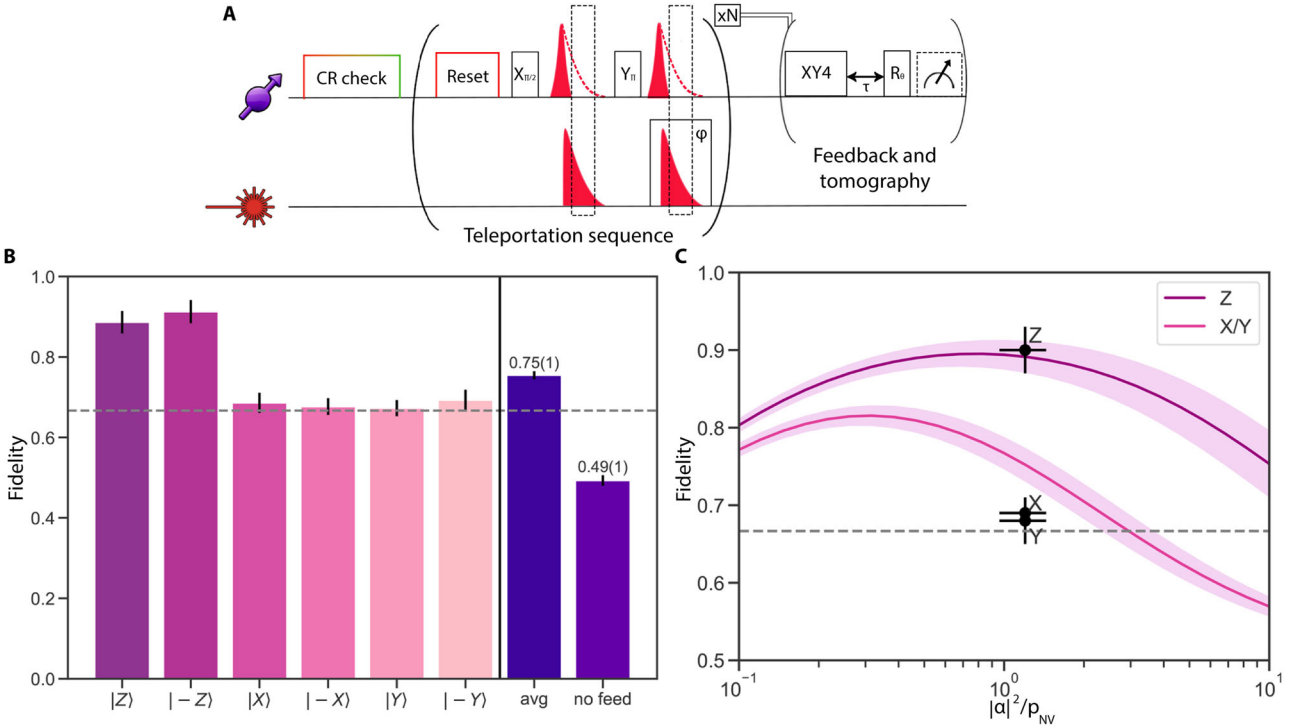

Fig. 4 | Quantum teleportation of a time-bin qubit into the electron spin of the NV center. A Experimental sequence. After passing the CR check, the AWG plays the teleportation sequence as described in the main text. Such a sequence is played N times. The timeout for the teleportation sequence is set to 50 repetitions, after which the NV center goes back to CR check. If a valid click pattern is detected by the FPGA in the Bell-state measurement, the AWG jumps out from the teleportation sequence and starts the feedback and tomography sequence. This sequence contains an XY4 set of pulses, where the first pulse is played after a time τ with respect to the $\pi/2$ rotation pulse in the teleportation sequence. The value τ is a multiple of the Larmor period of the electron spin, optimized taking into account the effects of the spin bath. After the XY4 sequence, the base selection pulse is played taking into account the input state and the Bell-state measurement outcome. Finally, the tomography single-shot readout of the NV electron spin is performed at the MCU level. **B** Histogram showing the individual fidelities per each cardinal state, as well as the average and the resulting fidelity when no feedback operations are applied to the NV electron spin qubit. The results are corrected for tomography errors, but not for preparation errors. **C** Simulation curves based on the model described in the SI. The data points in black represent the average fidelity for the states along the three axes of the Bloch sphere. The dashed line indicates the corrected classical bound.

Discussion

We have benchmarked a photonic interface between 795nm converted time-bin qubits and an NV center-based quantum processor. The time-bin qubits are compatible with Thulium-doped crystals employed for quantum memories as well as Rubidium gas quantum memories. The interface exhibits a high photon indistinguishability, thanks to a low-noise two-step quantum frequency conversion setup, that leads to beating the classical bound for the quantum teleportation protocol, together with the capabilities of the NV center as quantum processor, which shows long coherence time and a reliable optical interface. Additionally, the implementation of control scripts made the setup to be operable at distance and for long periods. Our results demonstrate the realization of interfaces between heterogeneous platforms that constitute the building blocks of the future Quantum Internet.

The interface presented in this work is versatile, as the methods and results presented can be transferred to platforms with similar functionalities. For emitters with different lifetimes, bandwidth matching needs to be considered by e.g. frequency filtering or emitter lifetime engineering in cavities via the Purcell effect. Additional improvements can be targeted at the application field (e.g. photonic clients protocols) and experimental rate. In regard to the latter, some examples might include the use of actual quantum memories that can be synchronized with the photon emission from the NV center, along with the integration of NV centers into optical cavities[37] for higher photon rate. Another possibility is the use of different color center defects in diamonds, like the group-IV, that promise higher photon emission rates and the possibility of integration into nanophotonic structures[38–41]. Other promising quantum processor platforms might include defect centers in SiC[42], Si[43] and optical quantum dots[4,44]. Additionally, higher efficiency frequency conversion setups to telecom wavelengths[45,46] can be employed to convert the photons emitted from both parties, leading towards the real-case scenario of quantum networks over long distances.

Methods

Fidelity calculation

The fidelity for each teleported state is calculated as $F = (1 + \frac{R_{\langle i|i\rangle} - R_{\langle j|i\rangle}}{R_{\langle i|i\rangle} + R_{\langle j|i\rangle}})/2$, given that we prepared the time-bin qubit in the state $|i\rangle$ and we measure in the state $|i\rangle$ and in its orthogonal state $|j\rangle$. The quantity $R_{\langle|\rangle}$ represents the tomography-related single-shot readout outcome, including the correction for known errors (see Supplementary of Ref. 10).

Data availability

The data used to produce the results in this manuscript are available at 4TU.ResearchData.

Received: 27 March 2024; Accepted: 22 October 2024;
Published online: 02 November 2024

References

1. Kimble, H. J. The quantum internet. *Nature* **453**, 1023–1030 (2008).
2. Wehner, S., Elkouss, D. & Hanson, R. Quantum internet: A vision for the road ahead. *Science* **362**, eaam9288 (2018).
3. Togan, E. et al. Quantum entanglement between an optical photon and a solid-state spin qubit. *Nature* **466**, 730–734 (2010).

4. Lodahl, P. Quantum-dot based photonic quantum networks. *Quantum Sci. Technol.* **3**, 013001 (2017).
5. Bock, M. et al. High-fidelity entanglement between a trapped ion and a telecom photon via quantum frequency conversion. *Nat. Commun.* **9**, 1998 (2018).
6. Ruf, M., Wan, N. H., Choi, H., Englund, D. & Hanson, R. Quantum networks based on color centers in diamond. *J. Appl. Phys.* **130**, 070901 (2021).
7. Stas, P.-J. et al. Robust multi-qubit quantum network node with integrated error detection. *Science* **378**, 557–560 (2022).
8. Lago-Rivera, D., Rakonjac, J. V., Grandi, S. & Riedmatten, H. D. Long distance multiplexed quantum teleportation from a telecom photon to a solid-state qubit. *Nat. Commun.* **14**, 1889 (2023).
9. Liu, J.-L. et al. Creation of memory–memory entanglement in a metropolitan quantum network. *Nature* **629**, 579–585 (2024).
10. Pompili, M. et al. Realization of a multinode quantum network of remote solid-state qubits. *Science* **372**, 259–264 (2021).
11. Hermans, S. L. N. et al. Qubit teleportation between non-neighbouring nodes in a quantum network. *Nature* **605**, 663–668 (2022).
12. Doherty, M. W. et al. The nitrogen-vacancy colour centre in diamond. *Phys. Rep.* **528**, 1–45 (2013).
13. Childress, L. & Hanson, R. Diamond NV centers for quantum computing and quantum networks. *MRS Bull.* **38**, 134–138 (2013).
14. Thiel, C., Sinclair, N., Tittel, W. & Cone, R. Tm3+:Y3Ga5O12 materials for spectrally multiplexed quantum memories. *Phys. Rev. Lett.* **113**, 160501 (2014).
15. Sinclair, N. et al. Proposal and proof-of-principle demonstration of non-destructive detection of photonic qubits using a Tm:LiNbO3 waveguide. *Nat. Commun.* **7**, 13454 (2016).
16. Askarani, M. F. et al. Long-lived solid-state optical memory for high-rate quantum repeaters. *Phys. Rev. Lett.* **127**, 220502 (2021).
17. Cho, Y.-W. et al. Highly efficient optical quantum memory with long coherence time in cold atoms. *Optica* **3**, 100–107 (2016).
18. Zhao, R. et al. Long-lived quantum memory. *Nat. Phys.* **5**, 100–104 (2009).
19. Rosenfeld, W., Berner, S., Volz, J., Weber, M. & Weinfurter, H. Remote preparation of an atomic quantum memory. *Phys. Rev. Lett.* **98**, 050504 (2007).
20. Heller, L., Farrera, P., Heinze, G. & de Riedmatten, H. Cold-atom temporally multiplexed quantum memory with cavity-enhanced noise suppression. *Phys. Rev. Lett.* **124**, 210504 (2020).
21. Azuma, K. et al. Quantum repeaters: From quantum networks to the quantum internet. *Rev. Mod. Phys.* **95**, 045006 (2023).
22. Drmota, P. et al. Verifiable blind quantum computing with trapped ions and single photons. *Phys. Rev. Lett.* **132**, 150604 (2024).
23. Bennett, C. H. et al. Teleporting an unknown quantum state via dual classical and Einstein-Podolsky-Rosen channels. *Phys. Rev. Lett.* **70**, 1895–1899 (1993).
24. Bouwmeester, D. et al. Experimental quantum teleportation. *Nature* **390**, 575–579 (1997).
25. Heshami, K. et al. Quantum memories: emerging applications and recent advances. *J. Mod. Opt.* **63**, 2005–2028 (2016).
26. Lei, Y. et al. Quantum optical memory for entanglement distribution. *Optica* **10**, 1511–1528 (2023).
27. Afzelius, M., Simon, C., de Riedmatten, H. & Gisin, N. Multimode quantum memory based on atomic frequency combs. *Phys. Rev. A* **79**, 052329 (2009).
28. Covey, J. P., Weinfurter, H. & Bernien, H. Quantum networks with neutral atom processing nodes. *npj Quantum Inf.* **9**, 1–12 (2023).
29. Lipka, M., Mazelanik, M., Leszczyński, A., Wasilewski, W. & Parniak, M. Massively-multiplexed generation of Bell-type entanglement using a quantum memory. *Commun. Phys.* **4**, 1–10 (2021).
30. Bussieres, F. et al. Prospective applications of optical quantum memories. *J. Mod. Opt.* **60**, 1519–1537 (2013).
31. Sangouard, N., Simon, C., de Riedmatten, H. & Gisin, N. Quantum repeaters based on atomic ensembles and linear optics. *Rev. Mod. Phys.* **83**, 33–80 (2011).
32. Kumar, P. Quantum frequency conversion. *Opt. Lett.* **15**, 1476–1478 (1990).
33. Hong, C. K., Ou, Z. Y. & Mandel, L. Measurement of subpicosecond time intervals between two photons by interference. *Phys. Rev. Lett.* **59**, 2044–2046 (1987).
34. Loudon, R.*The Quantum Theory of Light* (Clarendon Press, 1983).
35. Bernien, H. et al. Heralded entanglement between solid-state qubits separated by three metres. *Nature* **497**, 86–90 (2013).
36. Wang, Z.-H., de Lange, G., Ristè, D., Hanson, R. & Dobrovitski, V. V. Comparison of dynamical decoupling protocols for a nitrogen-vacancy center in diamond. *Phys. Rev. B* **85**, 155204 (2012).
37. Ruf, M., Weaver, M., van Dam, S. & Hanson, R. Resonant excitation and purcell enhancement of coherent nitrogen-vacancy centers coupled to a fabry-perot microcavity. *Phys. Rev. Appl.* **15**, 024049 (2021).
38. Hepp, C. et al. Electronic structure of the silicon vacancy color center in diamond. *Phys. Rev. Lett.* **112**, 036405 (2014).
39. Bhaskar, M. et al. Quantum nonlinear optics with a germanium-vacancy color center in a nanoscale diamond waveguide. *Phys. Rev. Lett.* **118**, 223603 (2017).
40. Nguyen, C. et al. Quantum network nodes based on diamond qubits with an efficient nanophotonic interface. *Phys. Rev. Lett.* **123**, 183602 (2019).
41. Rugar, A. E. et al. Quantum photonic interface for tin-vacancy centers in diamond. *Phys. Rev. X* **11**, 031021 (2021).
42. Lukin, D. M., Guidry, M. A. & Vučković, J. Integrated quantum photonics with silicon carbide: challenges and prospects. *PRX Quantum* **1**, 020102 (2020).
43. Higginbottom, D. B. et al. Optical observation of single spins in silicon. *Nature* **607**, 266–270 (2022).
44. Liu, S. et al. Violation of Bell inequality by photon scattering on a two-level emitter. *Nat. Phys.* https://www.nature.com/articles/s41567-024-02543-8 (2024).
45. Schäfer, M., Kambs, B., Herrmann, D., Bauer, T. & Becher, C. Two-stage, low noise quantum frequency conversion of single photons from silicon-vacancy centers in diamond to the telecom C-Band. *Adv. Quantum Technol.* https://onlinelibrary.wiley.com/doi/abs/10.1002/qute.202300228.
46. Bersin, E. et al. Telecom networking with a diamond quantum memory. *PRX Quantum* **5**, 010303 (2024).

Acknowledgements

We thank R.F.L. Vermeulen for designing and building the electronics for the frequency stabilization, P. Botma for help with the FPGA programming, K.L. van der Enden for experimental support, J.A. Slater for fruitful discussions. We acknowledge funding from the Dutch Research Council (NWO) through the Spinoza prize 2019 (project number SPI 63-264) and through the projects "QuTech Part I Fundamental research" (project number 601.QT.001-1) and "QuTech Part II Applied-oriented research" (project number 601.QT.001-2), and from the EU Flagship on Quantum Technologies through the project Quantum Internet Alliance (EU Horizon 2020, grant agreement no. 820445).

Author contributions

M.I., M.-C.S., A.J.S., M.J.W., W.T. and R.H. devised the experiments, M.I. and M.-C.S. carried out the experiments, collected and analyzed data and discussed the results with all authors. M.I., M.-C.S., A.J.S. and M.J.W. prepared the NV setup. M.I., M.-C.S, M.J.W, E.L., G.C.d.A. and M.O.S. designed, built and optimized the frequency conversion setups. M.I., M.-C.S., T.C., N.A. prepared the photonic time-bin qubit platform and integrated it in the setup. M.I. and R.H. wrote the main manuscript with input from all the authors and M.I and M.-C.S. wrote the Supplementary Information. R.H. and W.T. supervised the research.

Competing interests
The authors declare no competing interests.

Additional information
Supplementary information The online version contains supplementary material available at https://doi.org/10.1038/s41534-024-00910-0.

Correspondence and requests for materials should be addressed to Ronald Hanson.